

Analysis of Hydrodynamic Interactions during AFM Imaging of Biological Membranes

Tai-Hsi Fan and Andrei G. Fedorov*

Multiscale Integrated Thermofluidics Lab., G. W. Woodruff School of Mechanical Engineering, Georgia Institute of Technology, Atlanta, Georgia 30332-0405

Received July 31, 2002. In Final Form: November 27, 2002

The physical processes taking place during AFM imaging of soft biological membranes are investigated. A particular emphasis is placed on understanding of hydrodynamics effects in the fluid inside and outside of the cell associated with elastic deformation of the membrane in response to AFM tapping action for the entire probing cycle. For the first time, it is theoretically shown that "hysteresis" in the membrane deformation versus tip-sample separation curve is due to strong coupling of fluid motion and kinematics of the membrane bending for the noncontact mode of measurements in liquid environment. The effects of the AFM tip opening angle and the membrane elasticity constants such as bending rigidity and spontaneous curvature are investigated in detail to establish the structure of the flow field and dynamics of the membrane evolution, leading to theoretical interpretation of AFM imaging experiments.

1. Introduction

The atomic force microscope (AFM) provides a unique opportunity to investigate the spatially resolved structure, morphology, and mechanical properties of biological membranes down to the nanometer or atomic scale,¹ and these studies can be performed in-situ, that is, in a natural for cells aqueous environment. Examples of using an AFM in biology include investigation of the membrane structure, mechanical properties, and surface charge of living osteoblasts,^{2,3} measurement of molecular level interactions in microbial cells,⁴ and even assessment of electrically excited cardiac activities in living cells.^{5,6}

Mechanical properties of the cell membranes are typically deduced by generating an applied force versus distance curve when the AFM tip scans the surface and then fitting the experimental results to the simple Hertz model for the maximum distance between two elastically deformed surfaces.⁷ Further, to preserve the integrity of the biological sample under investigation, the tapping mode of operation is used by vibrating the AFM tip at high frequency during surface scanning. However, since biological membranes are highly deformable, fluidlike surfaces, the actual deformation of the membrane cannot be measured, thereby shading doubts on the validity of straightforward application of the Hertz model to deduce mechanical properties of the membrane. Indeed, a more detailed model is needed which accounts for interactions between an AFM tip and the membrane surface through hydrodynamic coupling via the fluid layer between the tip and membrane. Such a model would provide a fundamental basis for quantitative interpretation of AFM

imaging experiments as well as serve as a framework for designing new imaging modalities for noninvasive imaging of soft biological samples.

In this paper, we report development of the theoretical model and simulation results for fluid mechanics of the AFM imaging of biological membranes. The model couples dynamics of the biological membrane deformation and fluid motion inside and outside of the cell as the AFM tip probes the membrane interface in periodic tapping mode. The fluid motion is modeled by the Stokes creeping flow, and Helfrich's theory for the equilibrium shape of an infinitely thin biological membrane^{8,9} is used to determine an instantaneous position of the flexible boundary that links fluid flows inside and outside of the cell. The boundary element method¹⁰ is used as a numerical technique for computationally efficient solution of the problem. The results of simulations are intended to demonstrate the fundamental physics of what happens during AFM imaging of soft biological membranes as well as to assess the effect of main instrument/sample parameters (e.g., an AFM tip opening angle and the membrane elasticity constants such as bending rigidity and spontaneous curvature) on the force versus distance response curves generated in the AFM imaging experiments. The cell membrane behavior when an AFM tip moves in forward and reverse directions is also observed. The practical benefits from this research are twofold. First, the cell mechanical properties can be obtained from a modified hydrodynamic force versus distance curve without actually contacting or indenting the sample so that cell damage can be prevented. Second, the methodology to simulate the tip-sample interactions provides a theoretical foundation for interpretation of the convoluted experimental information obtained when multiple imaging functions are integrated into an AFM tip.¹¹

2. Formulation

2.1. Hydrodynamics Analysis. Figure 1 shows a schematic view of the AFM tip approaching a deformable

* To whom correspondence should be addressed. E-mail: andrei.fedorov@me.gatech.edu. Phone: 404-385-1356. Fax: 404-894-8496.

(1) Morris, V. J.; Kirby, A. R.; Gunning, A. P. *Atomic force microscopy for biologists*; Imperial College Press: 1999.

(2) Lee, I.; Marchant, R. E. *Colloids Surf., B* **2000**, 19, 357–365.

(3) Domke, J.; Dannöhl, S.; Parak, W. J.; Müller, O.; Aicher, W. K.; Radmacher, M. *Colloids Surf., B* **2000**, 19, 367–379.

(4) Dufrêne, Y. F.; Boonaert, C. J. P.; van der Mei, H. C.; Busscher, H. J.; Rouxhet, P. G. *Ultramicroscopy* **2001**, 86, 113–120.

(5) Domke, J.; Parak, W. J.; George, M.; Gaub, H. E.; Radmacher, M. *Eur. Biophys. J.* **1999**, 28, 179–186.

(6) Parak, W. J.; Domke, J.; George, M.; Kardinal, A.; Radmacher, M.; Gaub, H. E.; de Roos, A. D. G.; Theuvsen, A. P. R.; Wiegand, G.; Sackmann, E.; Behrends, J. C. *Biophys. J.* **1999**, 76, 1659–1667.

(7) Hertz, H. *J. Reine Angew Math.* **1881**, 92, 156–171.

(8) Helfrich, W. Z. *Naturforsch. Teil C* **1973**, 28, 693.

(9) Zhong-can, O.-Y.; Helfrich, W. *Phys. Rev. A* **1989**, 39, 5280–5288.

(10) Pozrikidis, C. *Boundary Integral and Singularity Methods for Linearized Viscous Flow*; Cambridge University Press: 1992.

(11) Kranz, C.; Friedbacher, G.; Mizaikoff, B. *Anal. Chem.* **2001**, 73, 2491–2500.

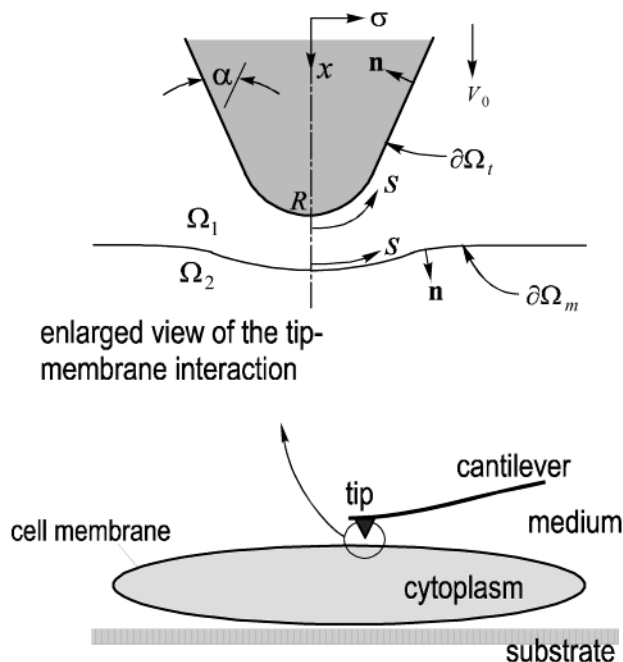


Figure 1. Schematic view of an AFM tip approaching a cell membrane and definition of the computational domain.

cell surface. The size of the biological cell is usually much larger than that of an AFM tip, so that a simplified representation with an initially planar membrane surface can be adapted. In a biological environment, the activities of microorganisms and living cells in the fluid are usually characterized by the low Reynolds number flow because of the small velocity and length scales. For example, the size of biological cells ranges from a few micrometers to several millimeters,¹² whereas the AFM tip is only tens to hundreds of nanometers in radius and up to several micrometers in height. Choosing the length scale as the height of an AFM tip, $L \sim 5 \mu\text{m}$, and assuming that the cell living environment is an aqueous solution with viscosity $\mu \sim 0.015 \text{ g/cm}\cdot\text{s}$ and density $\rho \sim 1.0 \text{ g/cm}^3$, the low Reynolds number criteria [$Re = \rho V_0 L / \mu \ll \mathcal{O}(1)$] are satisfied as long as the characteristic speed V_0 of an AFM tip is less than 1 cm/s ($Re \sim 0.03$). In AFM imaging, we assume that the tip-to-sample distance is of the order of $5 \mu\text{m}$ and the vertical scanning frequency is around $f \sim 10 \text{ Hz}$.² Thus, the resulting characteristic velocity $V_0 \sim 0.01 \text{ cm/s}$ is much less than the minimum velocity dictated by the low Reynolds number criteria for the Stokes flow; hence, the advection inertia force can be neglected. The characteristic time scale for the system is $\tau = 1/f \sim 0.1 \text{ s}$, leading to the forcing frequency parameter $\rho L^2 / \mu \tau$ of the order of 10^{-4} so that the acceleration force can also be neglected as compared to the viscous forces. Thus, the Stokes flow approximation is clearly justified for the system under consideration.

For simplicity, we assume that the fluids outside and inside the cell are incompressible Newtonian fluids with the same density and viscosity. A typical eukaryotic cell membrane with lipid bilayers and integrated glycoproteins is approximately 5 nm thick, so that the membrane thickness can be neglected in comparison to the size of an AFM tip. Thus, the membrane can be mathematically treated as an infinitesimally thin interface. Besides, for the continuous fluid representation to be applicable, the thermal fluctuations are assumed to be negligible so that

the membrane surface is perfectly smooth. We also assume that the system is isothermal, no other body forces are involved, and the cell membrane is nonpermeable. Furthermore, the molecular level interaction forces and the surface electrostatic force are not included in the analysis, as they become significant only at the tip-membrane separation around 50 nm or less. Specifically, the van der Waals, electrostatic double layer, and solvation forces are significant when the interface separation distance is less than 10 nm , and their effective range is rarely longer than 100 nm .¹³ Thus, neglecting molecular level interactions is justified in the present analysis, as it is correct to the order of magnitude of the AFM tip radius (500 nm).

On the basis of the Stokes flow approximation, the dynamics of both fluids, that is, inside (Ω_2 -domain) and outside (Ω_1 -domain) of the cell (Figure 1), is governed by the following momentum and mass conservation equations

$$\nabla \cdot \boldsymbol{\tau}(\mathbf{x}) = -\nabla p(\mathbf{x}) + \mu \nabla^2 \mathbf{u}(\mathbf{x}) = 0 \quad \text{for } \mathbf{x} \in \Omega_1 + \Omega_2 \quad (1)$$

$$\nabla \cdot \mathbf{u}(\mathbf{x}) = 0 \quad \text{for } \mathbf{x} \in \Omega_1 + \Omega_2 \quad (2)$$

respectively, where $\boldsymbol{\tau}$ is the viscous stress tensor, p is the hydrodynamic pressure, \mathbf{u} is the velocity field vector, μ is the dynamic viscosity assumed constant, and \mathbf{x} denotes a position vector in the Cartesian coordinate system. The kinematic boundary conditions for the flow field are no-slip at both the AFM tip and the membrane surfaces,

$$\mathbf{u}(\mathbf{x}) = V_0 \hat{\mathbf{e}}_x \quad \text{for } \mathbf{x} \in \partial\Omega_t \quad (3)$$

$$\mathbf{u}(\mathbf{x}) = \mathbf{u}_m \quad \text{for } \mathbf{x} \in \partial\Omega_m \quad (4)$$

where V_0 is a prescribed approach speed of the AFM tip, $\hat{\mathbf{e}}_x$ is the unit vector along the x -axis direction (Figure 1), and \mathbf{u}_m is an unknown local migration velocity of the cell membrane. The rest of the unbounded fluid domain is assumed quiescent at infinity. The solution of eqs 1 and 2 requires knowledge of the position of the cell membrane, which, in turn, is defined by the AFM induced flow in domains Ω_1 and Ω_2 (Figure 1), according to the migration velocity, which is not known a priori. Thus, to complete formulation of the problem, a dynamic boundary condition is required to couple the fluid motion on both sides of the cell membrane to determine migration of the membrane due to the hydrodynamic and membrane elasticity effects. This dynamic boundary condition can be obtained from the stress balance on both sides of the membrane, and it is discussed in detail in section 2.2.

Although the problem in hand is a transient nonlinear problem owing to an a priori unknown deformation of the cell membrane, the governing equations (1 and 2) are those for the simplified linear, quasi-steady Stokes flow. Thus, the problem can be solved by the general solution procedure for the Stokes flows,¹⁰ while satisfying the nonlinear boundary condition at the cell membrane via numerical iterations. A convenient way to solve the linearized fluid flow problem is by using the boundary integral method, which originates from the Lorentz reciprocal theorem¹⁴ in 1907. The integral solution of the Stokes flow problem was later outlined by Odqvist¹⁵ and Ladyzhenskaya¹⁶ by considering the solution as superposition of the contribu-

(13) Israelachvili, J. N. *Intermolecular and Surface Forces*; Academic Press: San Diego, CA, 1998.

(14) Lorentz, H. A. *Abh. Theor. Phys.* **1907**, 1, 23–42.

(15) Odqvist, F. K. G. *Math. Z.* **1930**, 32, 329–375.

(16) Ladyzhenskaya, O. A. *The Mathematical Theory of Viscous Incompressible Flow*; Gordon & Breach: New York, 1969.

(12) Alberts, B.; et al. *Molecular biology of the cell*; Garland Pub.: New York, 1994.

tions from single layer (the flow induced by the continuously distributed point force, Stokeslet) and double layer (the flow induced by the continuous point stress, Stresslet) potentials. The details of the theoretical development and numerical implementation of the integral formulation are discussed in detail by Pozrikidis.¹⁰ The Lorentz reciprocal theorem gives a pairwise relation between the real flow in the actual physical domain and the Stokeslet flow induced by the corresponding Green's function. Following Pozrikidis' derivation,¹⁰ a general integral solution of the Stokes flow problem satisfies the following boundary integral equation:

$$\int_{\partial\Omega} [\tau_{ik}(\mathbf{x}) G_{ij}(\mathbf{x}, \mathbf{x}_0) - \mu u_i(\mathbf{x}) T_{ijk}(\mathbf{x}, \mathbf{x}_0)] n_k(\mathbf{x}) dA(\mathbf{x}) = 0 \quad (5)$$

where the singular source point is located outside the fluid domain, $\mathbf{x}_0 \notin \Omega$, the unit surface normal vector n_k points into the fluid domain, u_i and τ_{ik} represent the physical velocity and stress fields, respectively, and the fundamental solution (Stokeslet) and its corresponding stress field (Stresslet) are given by

$$G_{ij}(\mathbf{x}, \mathbf{x}_0) = \frac{\delta_{ij}}{r} + \frac{r_i r_j}{r^3} \quad \text{and} \quad T_{ijk}(\mathbf{x}, \mathbf{x}_0) = -6 \frac{r_i r_j r_k}{r^5} \quad (6)$$

respectively, where δ_{ij} is the Kronecker delta function, $\mathbf{r} = \mathbf{x} - \mathbf{x}_0$ is the position vector between the given field point and a source point, and $r = |\mathbf{x} - \mathbf{x}_0|$ is the distance between them. When the source point is located inside the flow field, $\mathbf{x}_0 \in \Omega - \partial\Omega$, the combined Stokeslet and Stresslet induced velocity field must satisfy the following general integral solution:

$$u_j(\mathbf{x}_0) = -\frac{1}{8\pi\mu} \int_{\partial\Omega} \tau_{ik}(\mathbf{x}) n_k(\mathbf{x}) G_{ij}(\mathbf{x}, \mathbf{x}_0) dA(\mathbf{x}) + \frac{1}{8\pi} \int_{\partial\Omega} u_i(\mathbf{x}) T_{ijk}(\mathbf{x}, \mathbf{x}_0) n_k dA(\mathbf{x}) \quad (7)$$

An integral formulation of the Stokes flow problem for the two-fluid system with a free moving interface has been studied previously for fluids with arbitrary viscosity ratio.^{17–19} We use this technique to find the surface force jump condition in the case when the viscosity ratio is unity, resulting in vanishing of the double layer integral at the surface of the cell membrane. To simplify notation, the traction term is replaced by the surface force expression, $f_i = \tau_{ik} n_k$, and the obvious position symbols are dropped hereafter in this paper. Applying eq 7 to fluid 2 (inside of the cell) and eq 5 to fluid 1 (outside of the cell) and then combining the resulting equations, the flow field inside of the cell (domain Ω_2) can be expressed in terms of the surface force jump, $\Delta f_i = f_i^{(2)} - f_i^{(1)}$

$$u_j^{(2)} = -\frac{1}{8\pi\mu} \int_{\partial\Omega_m} \Delta f_i G_{ij} dA + \frac{1}{8\pi\mu} \int_{\partial\Omega_t} f_i^{(1)} G_{ij} dA - \frac{1}{8\pi} \int_{\partial\Omega_t} u_i^{(1)} T_{ijk} n_k dA \quad (8)$$

with Δf_i becoming the source density acting on fluid 2 from the cell membrane surface. Here, $\partial\Omega_m$ and $\partial\Omega_t$ denote the surfaces of the cell membrane and of the AFM tip, respectively, and the superscripts (1) and (2) refer to the fluid domains outside (Ω_1) and inside (Ω_2) of the cell, respectively. Note that eq 8 is still valid even when the

source point \mathbf{x}_0 is approaching the membrane surface, since the improper double layer integral ($\int_{\partial\Omega_m} u_i T_{ijk} n_k dA$) vanishes. Similar arguments can be applied to develop an integral momentum conservation equation for the fluid 1 outside of the cell,

$$u_j^{(1)} = -\frac{1}{8\pi\mu} \int_{\partial\Omega_m} \Delta f_i G_{ij} dA + \frac{1}{8\pi\mu} \int_{\partial\Omega_t} f_i^{(1)} G_{ij} dA - \frac{1}{8\pi} \int_{\partial\Omega_t} u_i^{(1)} T_{ijk} n_k dA \quad (9)$$

An improper integral of the double layer potential (the third term in eq 9) is interpreted in the sense of the Cauchy principal value when the source point is approaching the AFM tip surface, where we have

$$\lim_{\mathbf{x}_0 \rightarrow \partial\Omega_t} \int_{\partial\Omega_t} u_i^{(1)} T_{ijk} n_k dA = -4\pi u_j + \int_{\partial\Omega_t}^{p.v.} u_i^{(1)} T_{ijk} n_k dA \quad (10)$$

To generalize the approach, we render the governing equations dimensionless by describing the fluid motion and membrane dynamics using the following scales: length scale is given by the AFM tip radius R , velocity is scaled by the tip approach velocity V_0 , time is scaled by R/V_0 , the local surface tension γ is scaled by $V_0\mu$, the membrane bending rigidity B is scaled by $V_0\mu R^2$, the membrane mean curvature H and the spontaneous curvature c_0 are scaled by $1/R$, the Gaussian curvature K is scaled by $1/R^2$, and the surface force f and pressure p are both scaled by $V_0\mu/R$. Using these scales, the dimensionless integral form of the governing equations (8 and 9) becomes

$$\lambda u_j = -\frac{1}{8\pi} \int_{\partial\Omega_m} \Delta f_i G_{ij} dA + \frac{1}{8\pi} \int_{\partial\Omega_t} f_i^{(1)} G_{ij} dA - \frac{1}{8\pi} \int_{\partial\Omega_t}^{p.v. \text{ for } \mathbf{x}_0 \in \partial\Omega_t} u_i T_{ijk} n_k dA \quad (11)$$

where

$$\lambda = \begin{cases} 1 & \text{for } \mathbf{x}_0 \in \Omega_1 + \Omega_2 + \partial\Omega_m \\ 1/2 & \text{for } \mathbf{x}_0 \in \Omega_t \end{cases} \quad (12)$$

with the boundary conditions

$$\mathbf{u}(\mathbf{x}) = 1\hat{\mathbf{e}}_x \quad \text{for } \mathbf{x} \in \Omega_t, \quad \mathbf{u}(\mathbf{x}) = \mathbf{u}_m \quad \text{for } \mathbf{x} \in \partial\Omega_m, \\ \mathbf{u}(\mathbf{x}) = 0 \quad \text{for } \mathbf{x} \rightarrow \infty \quad (13)$$

Since the AFM tip, the cell membrane, and induced flow are axisymmetric, the surface integrals in eq 11 can be reduced to the line integrals by transforming the Cartesian coordinates to the polar cylindrical coordinates through $(x, y, z) = (x, \sigma \cos \phi, \sigma \sin \phi)$ and then integrating eq 11 along the azimuthal ϕ direction. As shown in Figure 1, x is the coordinate along the axial direction, σ is the coordinate along the radial direction, and ϕ is the azimuthal angle. The integral eq 11 is reduced to one-dimensional form by using the integral over the arc length s along the membrane boundary within a vertical plane defined by the constant azimuthal angle. The transformed integral equation is then expressed as

$$\lambda u_\alpha = -\frac{1}{8\pi} \int_{\partial\Omega_m} M_{\alpha\beta} \Delta f_\beta ds + \frac{1}{8\pi} \int_{\partial\Omega_t} M_{\alpha\beta} f_\beta^{(1)} ds - \frac{1}{8\pi} \int_{\partial\Omega_t}^{p.v. \text{ for } \mathbf{x}_0 \in \partial\Omega_t} Q_{\alpha\beta\gamma} u_\gamma n_\beta ds \quad (14)$$

where λ is defined in eq 12, the Greek symbols α, β , and

(17) Rallison, J. M.; Acrivos, A. *J. Fluid Mech.* **1978**, *89*, 191–200.

(18) Lee, S. H.; Leal, L. G. *J. Colloid Interface Sci.* **1982**, *87*, 81–106.

(19) Pozrikidis, C. *J. Fluid Mech.* **1990**, *210*, 1–21.

γ denote either x or σ directions, and the kernel functions $M_{\alpha\beta}$ and $Q_{\alpha\beta\gamma}$ are the transformation matrices from Stokeslet and Stresslet in the Cartesian coordinate system.^{10,17} Each matrix element in $M_{\alpha\beta}$ and $Q_{\alpha\beta\gamma}$ can be determined in terms of the complete elliptic integrals of the first and second kind and is either approximated by the asymptotic polynomials or computed by direct numerical integration. The details of transformations are given in the Appendix for completeness.

2.2. Deformation of the Biological Membrane.

Unlike the free interface between two immiscible fluids, mammalian cell membranes are constructed by amphiphilic molecules such as phospholipids or glycolipids with integrated functional proteins. The flexible and fluidlike lipid bilayers form an elastic interface which can resist bending and stretching to maintain the integrity of the membrane surface.²⁰ Since the lipid molecules are free to migrate or rearrange locally within the surface of the fluidlike membrane, the surface tension could be assumed locally isotropic on the time scale of interest in this study as long as the lipid bilayer has negligible shear elasticity and the membrane deformation is dominated by its bending rigidity. Considering a dynamic boundary condition for the surface force jump in a three-dimensional free surface flow, a postulation generalized by Landau²¹ and Scriven²² takes the form

$$(\mathbf{r}_2 \cdot \mathbf{n} - \mathbf{r}_1 \cdot \mathbf{n}) + \nabla_s \gamma - \gamma \mathbf{n}(\nabla_s \cdot \mathbf{n}) = 0 \quad (15)$$

where $\mathbf{r}_2 \cdot \mathbf{n} - \mathbf{r}_1 \cdot \mathbf{n}$ is the net surface traction acting along the surface normal \mathbf{n} and tangent \mathbf{t}_s directions, ∇_s is a surface gradient operator, and γ is the surface tension. For a fluidlike membrane characteristic to cells, the normal force component ($\gamma \nabla_s \cdot \mathbf{n}$) in eq 15 has to be generalized using the fluid membrane theory originated from Helfrich;⁸ see also ref 23 in conjunction with a more recently developed equation for the equilibrium shape of a vesicle membrane.^{9,24,25} It is now known that the major factor that defines an equilibrium shape of the cell membranes is the bending stiffness,²⁶ and the equilibrium membrane shape of a spherical vesicle is determined by the minimization of the curvature free energy, or shape energy²⁵

$$E = \frac{1}{2} B \int (c_1 + c_2 - c_0)^2 dA + \Delta p \int dV + \int \gamma dA \quad (16)$$

where B is the apparent bending rigidity, c_1 and c_2 are the two principal curvatures, c_0 is the effective spontaneous curvature that is used to describe various asymmetric effects in the membrane itself and its living environment,²⁶ $\Delta p = p_{\text{out}} - p_{\text{in}}$ is the osmotic pressure difference between outer and inner fluids of the cell, γ is the local surface tension, and $\int(\dots) dV$ and $\int(\dots) dA$ are integrals over the volume and surface of the cell, respectively. Taking the first variation of the shape energy given by eq 16, and treating Δp and γ as the Lagrange multipliers for the volume and surface constraints, respectively, Zhong-can and Helfrich²⁴ derived the equilibrium shape equation for the vesicle membranes

$$\Delta p - 2\gamma H + B(2H + c_0)(2H^2 - 2K - c_0 H) + 2B\nabla^2 H = 0 \quad (17)$$

where $H = -(c_1 + c_2)/2$ is the mean curvature, $K = c_1 c_2$ is the Gaussian curvature, and ∇^2 is the Laplace–Beltrami operator for the curvilinear surface. In a dynamic system such as an AFM cell membrane immersed into a liquid, the viscous effects associated with motion of fluids on both sides of the interface must be included in eq 17 to describe the surface force jump across the cell membrane. Thus, the balance of the normal force has to be generalized to obtain a Laplace-like formula, as shown by Zhong-can,²⁵

$$(\mathbf{r}_2 \cdot \mathbf{n} - \mathbf{r}_1 \cdot \mathbf{n}) = [\Delta p - 2\gamma H + B(2H + c_0)(2H^2 - 2K - c_0 H) + 2B\nabla^2 H] \quad (18)$$

Assuming that the initial osmotic pressure difference Δp is zero for the planar membrane interface, the dynamic boundary condition (eq 15) can be modified as follows:

$$\Delta \mathbf{f} = [-2\gamma H + B(2H + c_0)(2H^2 - 2K - c_0 H) + 2B\nabla^2 H] \mathbf{n} - \nabla_s \gamma \quad (19)$$

where $\Delta \mathbf{f} = \mathbf{r}_2 \cdot \mathbf{n} - \mathbf{r}_1 \cdot \mathbf{n}$ enters the Stokes system describing fluid motion through eq 14.

In the free surface problems, the surface force jump $\Delta \mathbf{f}$ is solely determined by the surface geometry. For the flexible membrane, however, eq 19 shows that the local tension force γ must be known a priori in order to determine the surface force jump. Thus, an additional equation needs to be introduced based on the membrane surface constraint to complete the formulation. From differential geometry, the two surface curvilinear coordinates ξ and η can be introduced to describe the position vector $\mathbf{r}(\xi, \eta)$ defining the membrane surface. There exist two tangential vectors and the surface normal defined by

$$\mathbf{r}_\xi = \partial \mathbf{r} / \partial \xi, \quad \mathbf{r}_\eta = \partial \mathbf{r} / \partial \eta, \quad \mathbf{n} = (\mathbf{r}_\xi \times \mathbf{r}_\eta) / |\mathbf{r}_\xi \times \mathbf{r}_\eta| \quad (20)$$

and a useful covariant metric tensor defined for the general curvilinear system by

$$g_{ij} = \mathbf{r}_i \cdot \mathbf{r}_j \quad (21)$$

where i and j are either the ξ or η directions. In the case of a locally incompressible cell membrane, the surface area must remain locally constant in time so that the dilation rate of a differential surface element satisfies the constraint

$$\frac{\partial(dA)}{\partial t} = \frac{\partial}{\partial t} \int \sqrt{g} d\xi d\eta = 0 \quad (22)$$

with the 2-D Jacobian of the transformation given by

$$\sqrt{g} = \sqrt{\det(g_{ij})} = |\mathbf{r}_\xi \times \mathbf{r}_\eta| \quad (23)$$

Then eq 22 can be written in differential form

$$\mathbf{n} \cdot \frac{\partial}{\partial t} (\mathbf{r}_\xi \times \mathbf{r}_\eta) = 0 \quad (24)$$

Using the orthogonal curvilinear surface coordinates, that is, the arc length s and the azimuthal angle ϕ , as ξ and η , respectively, the time derivative of eq 24 can be expressed in terms of components of the surface migration velocity \mathbf{u} ,

(20) Evans, E. A.; Skalak, R. *Mechanics and Thermodynamics of Biomembranes*; CRC Press: Boca Raton, FL, 1980.

(21) Landau, L. D.; Lifshitz, E. M. *Fluid Mechanics*; Pergamon Press: London, 1959.

(22) Scriven, L. E. *Chem. Eng. Sci.* **1960**, *12*, 98–108.

(23) Deuling, H. J.; Helfrich, W. *J. Phys. (Paris)* **1976**, *37*, 1335.

(24) Zhong-can, O.-Y.; Helfrich, W. *Phys. Rev. Lett.* **1987**, *59*, 2486–2488.

(25) Zhong-can, O.-Y. *Thin Solid Films* **2001**, *393*, 19–23.

(26) Döbereiner, H. G. *Curr. Opin. Colloid Interface Sci.* **2000**, *5*, 256–263.

$$\mathbf{n} \cdot [\mathbf{u}_s \times \mathbf{r}_\phi + \mathbf{r}_s \times \mathbf{u}_\phi] = 0 \quad (25)$$

For $\mathbf{r} = (x, \sigma \cos \phi, \sigma \sin \phi)$ and $\mathbf{u} = (u_x, u_\sigma \cos \phi, u_\sigma \sin \phi)$, one can relate the unit tangent vector \mathbf{t}_s along the arc length coordinate s to the surface normal \mathbf{n} by

$$\mathbf{t}_s = -n_\sigma \hat{\mathbf{e}}_x + n_x \hat{\mathbf{e}}_\sigma \quad (26)$$

With that, we can further simplify eq 25 to obtain

$$\sigma \mathbf{t}_s \cdot \frac{\partial \mathbf{u}}{\partial s} + \mathbf{u} \cdot \hat{\mathbf{e}}_\sigma = 0 \quad (27)$$

Note that eq 27 is consistent with the Pozrikidis derivation for a nonisotropic stretching membrane by considering the constraint of the principal extension ratios.²⁷ Substituting eq 14 into eq 27 for $\mathbf{x}_0 \in \Omega_m$, we obtain the membrane area constraint in the final compact form,

$$\begin{aligned} & \int_{\partial\Omega_m} \left(\sigma(\mathbf{x}_0) t_\alpha(\mathbf{x}_0) \frac{\partial M_{\alpha\beta}(\mathbf{x}, \mathbf{x}_0)}{\partial s(\mathbf{x}_0)} + M_{\alpha\beta}(\mathbf{x}, \mathbf{x}_0) \right) \Delta f_\beta(\mathbf{x}) \, ds(\mathbf{x}) - \\ & \int_{\partial\Omega_i} \left(\sigma(\mathbf{x}_0) t_\alpha(\mathbf{x}_0) \frac{\partial M_{\alpha\beta}(\mathbf{x}, \mathbf{x}_0)}{\partial s(\mathbf{x}_0)} + M_{\alpha\beta}(\mathbf{x}, \mathbf{x}_0) \right) f_\beta^{(1)}(\mathbf{x}) \, ds(\mathbf{x}) + \\ & \int_{\partial\Omega_i} \left(\sigma(\mathbf{x}_0) t_\alpha(\mathbf{x}_0) \frac{\partial Q_{\alpha\beta\gamma}(\mathbf{x}, \mathbf{x}_0)}{\partial s(\mathbf{x}_0)} + Q_{\alpha\beta\gamma}(\mathbf{x}, \mathbf{x}_0) \right) u_\gamma(\mathbf{x}) n_\beta(\mathbf{x}) \, ds(\mathbf{x}) = 0 \quad (28) \end{aligned}$$

where α and β denote either the σ or x directions, and the unknown local tension force γ can be obtained implicitly from $\Delta \mathbf{f}$ given by eq 19.

In summary, we have developed the linear integral equations (14 and 28) for the boundary value problem that, combined with the flow boundary conditions given by eq 13 and the nonlinear interface boundary condition of eq 19 defining the surface force jump as a function of the membrane geometry and the local surface tension, describes the flow of fluids inside and outside of the cell as well as membrane deformation during the AFM imaging process.

3. Numerical Method

The coupled fluid–membrane system is solved using the boundary element method (BEM) with discretization along the surfaces of the AFM tip and the cell membrane. One advantage of this method is that no discretization of governing equations is needed inside the solution domain, but only along the boundaries. Once the boundary values are obtained, the field solutions (i.e., inside the domain) can be obtained through simple and computationally efficient postprocessing calculations. Also, for the axisymmetric formulation, the dimensionality is further reduced to a one-dimensional problem, which significantly simplifies the solution of the problem.

The model is described by four integral equations (eq 14, given that α denotes two directions, x and σ , and λ is defined by eq 12), and subject to one constraint integral equation (eq 28) for total five unknown functions. $u_x(\mathbf{x})$ and $u_\sigma(\mathbf{x})$ for $\mathbf{x} \in \partial\Omega_m$, $f_x(\mathbf{x})$ and $f_\sigma(\mathbf{x})$ for $\mathbf{x} \in \partial\Omega_i$, and $\gamma(\mathbf{x})$ for $\mathbf{x} \in \partial\Omega_m$. The calculations use N_t and N_m collocation points for the AFM tip and the cell membrane, respectively. After discretization and numerical approximation of the integral equations, there are a total of $2N_t + 3N_m$ linear algebraic equations to be solved simultaneously at each time step. The initial state assumes that the membrane is planar and the AFM tip to membrane separation distance is $10R$ (recall that R is the radius of the AFM

tip). The position of an AFM tip and that of the cell membrane are advanced following the local velocity field at every time step using the Euler time integration method for each collocation point.²⁸ On the fluid membrane, the collocation points are rearranged at every time step by cubic spline interpolation with node clustering near the membrane center, while maintaining the total number of elements fixed. Observing that the decay of the Green's function is of the order of $(1/r)$, and that of the Stresslet is of the order of $(1/r^2)$, the surface integrals can be truncated without loss of accuracy at sufficiently large r . Although the membrane area also increases proportional to r , the truncation is still justified in evaluation of the first integral term in eq 11 because the surface curvatures (H and K) and the gradient of the surface tension $\nabla_s \gamma$ vanish at large distances r where the membrane becomes planar, resulting in fast decay of the surface force jump Δf_i with the distance r according to eq 19. In numerical calculations, we truncate the integral at the dimensionless radius $\sigma \approx 150$. The appropriate truncation distance is justified through sensitivity studies. The element level integral is evaluated by the Gaussian quadrature,²⁸ and the system of algebraic equations is solved by the Gauss elimination method.²⁸

Further, if we assume that the local membrane tension force γ is isotropic, the tangent component of the interface stress in eq 19 can be expressed in terms of an arc-length coordinate s as follows:

$$\nabla_s \gamma = \frac{\partial \gamma}{\partial s} \mathbf{t}_s \quad (29)$$

Since γ is an unknown, this surface gradient operation is implemented in an implicit finite difference form to achieve the numerical stability. The derivatives of the transformation matrices $\partial M_{\alpha\beta}/\partial s$ and $\partial Q_{\alpha\beta\gamma}/\partial s$ in eq 28 are evaluated by the central difference at the integration points. In general, the membrane boundary can be defined by the parametric equations, $x = x(s)$ and $\sigma = \sigma(s)$ with s being the arc-length along the membrane interface $\partial\Omega_m$ measured from the center point (Figure 1). From differential geometry, the parametric forms for the mean curvature H and Gaussian curvature K are derived:

$$H(x(s), \sigma(s)) = \text{sign}(x') \frac{\sigma \sigma' x'' + x'^3 + (\sigma'^2 - \sigma' \sigma'') x'}{\sigma} \quad (30)$$

$$K(x(s), \sigma(s)) = \frac{\sigma' x' x'' - \sigma'' x'^2}{\sigma} \quad (31)$$

Also, the Laplace–Beltrami term in eq 19 can be expressed in terms of the arc-length coordinate s as

$$\nabla^2 H = \frac{\partial^2 H}{\partial s^2} \quad (32)$$

In the evaluation of membrane curvatures in eqs 30 and 31, the continuous first- and second-order derivatives of $x(s)$ and $\sigma(s)$ along the arc-length are evaluated on a cubic spline. The mean curvature $H(s)$ may exhibit small oscillations in the second-order derivatives which prohibit the Laplacian operation in eq 32. A remedial way to increase the smoothness of the mean curvature is to use the piecewise polynomial fit along the arc-length s in the least-squares sense²⁸ and to compute the Laplacian directly from the polynomial representation. Numerical test

(27) Pozrikidis, C. *J. Fluid Mech.* **1990**, *216*, 231–254.

(28) Press, W. H.; Teukolsky, S. A.; Vetterling, W. T.; Flannery, B. P. *Numerical Recipes in C: The Art of Scientific Computing*; Cambridge University Press: New York, 1988.

showed that a third-order piecewise polynomial with between six and twelve point window size can filter out the small oscillation in $H(s)$.

It should be noted that the mathematical developments above assume that all functions and their derivatives are sufficiently smooth to perform the differential operations. Besides, the uniqueness of the solution of the coupled integral equations (14 and 28) cannot be easily proven, since the unknown local membrane tension γ is defined as a Lagrange multiplier which may render multiple solutions of the problem. Our numerical experiments show that multiple converged solutions for γ do indeed exist, but the physically plausible solution is the one that results in $\gamma = 0$ at $\sigma \rightarrow \infty$, that is, at the truncated membrane location, or an a priori known constant value for the planar membrane at the initial stage.

4. Simulation Results

We consider three basic interaction processes in respect to direction of the tip movement to characterize the fundamental modes of tip–membrane interactions in noncontact tapping mode: first, the AFM tip is approaching an initially planar membrane with a constant velocity in the positive x direction (*forward*) until the tip–membrane separation distance is equal to R (where R is the tip radius); second, the tip returns to its initial position, moving in the negative x direction (*reverse*); and third, the tip stops at its upper state and the membrane is allowed to freely relax and slowly return to its undeformed planar shape (*relaxation*). It should be noted that the driving mechanisms for the membrane deformation are different from those responsible for the free liquid–liquid interface evolution¹⁸ because of the additional effects arising from the surface bending energy and the local tension or compression force induced by the constant area constraint, reflecting the assumption of the local membrane incompressibility. Although an harmonic, rather than a piecewise-constant-velocity, motion of the cantilever is a more realistic representation of the actual AFM tapping-mode operation, the main goal of this article is to uncover fundamental modes of fluid–membrane interactions under conditions which are relevant, but not necessarily identical, to current practices of using an AFM for imaging soft samples. Indeed, the tip acceleration/deceleration under the harmonic cantilever motion will only convolute the insight into the basic physics of the problem, and simplified cantilever motion with a piecewise constant velocity provides an opportunity to reveal the key physical mechanisms of the AFM imaging process necessary for understanding and optimization of the process. Thus, because of the overwhelming complexity of the problem, our main goal here is to gain a fundamental insight and resolve key interaction mechanisms independently, and we plan to investigate the harmonic tapping-mode cantilever dynamics in full detail in the follow-up studies.

The results of presented simulations are based on the geometry of the computational domain defined by the following dimensionless quantities: the AFM tip height is $10R$, the initial tip–sample separation is $10R$, and the dimensionless time step is set to 0.1 and is increased to 2.0 in the final stage of the slow membrane relaxation. Several test cases with the dimensionless bending rigidity B varying from 0.1 to 20.0, the tip opening angle ranging from 15° to 90° , and the spontaneous curvature c_0 changing from -0.1 to -5.0 are investigated by comparing corresponding force versus distance response curves. In all reported simulations, a total of 40 boundary elements are used for the tip and 60 elements are used for the cell

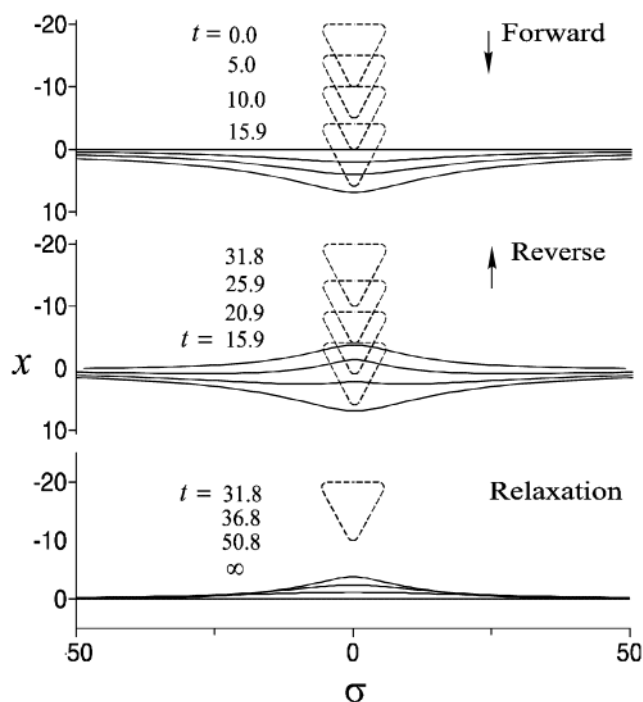


Figure 2. Full cycle evolution of the fluid membrane with bending rigidity $B = 1.0$ and spontaneous curvature $c_0 = -2.0$ induced by the AFM tip with an opening angle $\alpha = 60^\circ$.

membrane with element clustering around the center portion where the deformation is more significant. This set of simulation parameters was selected after an extensive grid sensitivity study based on its ability to produce the mesh-independent results with temporal and spatial resolutions sufficient for capturing the essential details of the system dynamics.

Figure 2 shows the membrane evolution during forward, reverse, and relaxation modes of AFM imaging. As a result of viscous flow induced by an AFM motion in fluid outside of the cell, the membrane is pushed forward (bends down) by the hydrodynamic piston force, and the fluid within the cell is in turn moved by the membrane with the highest local velocity around the center location. The curvature-dependent bending energy continuously changes with the membrane bending, thereby providing a local resistance to any deformation away from the planar, equilibrium state of the membrane of the minimum energy. This resistance causes different transient behavior during forward and reverse modes of AFM operation. In the *forward* (push) motion mode, an increase in the bending energy induces upward motion of the fluid above the membrane (negative local migration velocities of fluid 1) against the hydrodynamic (forward directed) forces. On the other hand, in the *reverse* (pull) mode of operation, a decrease in the bending energy assists initially the membrane to withdraw from its highly deformed, bend-down state. However, once the membrane returns to and passes its equilibrium planar position going upward, the bending energy again starts increasing and begins to resist any further deformation of the membrane until the membrane reaches its maximum negative deformation when the AFM tip stops in its upper position. In the final *relaxation* stage, the migration of the membrane is slow and solely depends on its bending energy and the fluid viscosity. The evolution shows that the viscous hydrodynamic forces affect the membrane state even in the far field along the radial direction, which is a typical dragging behavior of the Stokes flows. If the simulations are continued for a sufficiently long time, the membrane eventu-

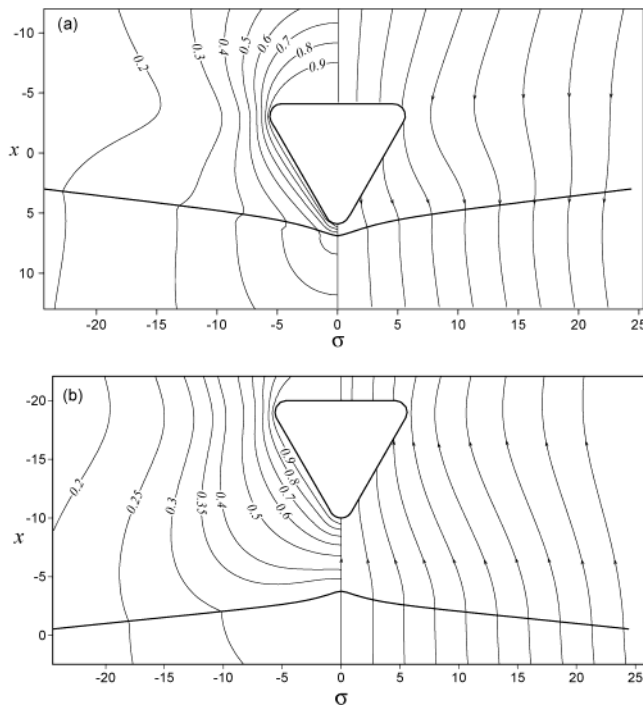


Figure 3. Instantaneous normalized velocity contours (left) and streamlines (right) around the AFM tip and the cell membrane at the following time instants: (a) $t = 15.9$ in the forward direction; (b) $t = 31.8$ in the reverse direction for the membrane with bending rigidity $B = 1.0$, spontaneous curvature $c_0 = -2.0$, and the AFM tip with an opening angle $\alpha = 60^\circ$.

ally returns to its equilibrium planar shape and the fluid velocity, the hydrodynamic forces, and the membrane surface forces vanish everywhere.

Figure 3 shows the axisymmetric streamlines and contours of the velocity field at the end of the forward and reverse motion of the AFM tip at time moments $t = 15.9$ and 31.8 , respectively, for $B = 1.0$, $c_0 = -2.0$, and $\alpha = 60^\circ$. The velocity field is computed as a postprocessing step using eq 14 with $\lambda = 1.0$ after the boundary values of the velocity are calculated. The velocity field reveals the kinematics of the flow produced by the coupling effects of the AFM tip motion and elastic deformation of the cell membrane. A relatively high speed flow is induced in the wake behind the flat bottom area of the AFM tip due to the strong viscous dragging force from the bottom surface and a relatively weak response from the membrane. Right near the front of the AFM tip and around the cone-shaped surface of the tip, the induced flow field is suppressed by the strong opposite single-layer force potential distributed along the surface of the deformed membrane. As a result, the velocity magnitude is reduced but the local velocity gradient becomes greater. The moving tip causes a converging/diverging streamline pattern around the tip circumference, which is the behavior generally observed in the Stokes flows when the flow field is perturbed by a moving body of an arbitrary shape. The contours show that the velocity field decays significantly along the radial σ -axis away from the centerline, which supports our choice of truncating the computational domain along the membrane at $\sigma = 150R$. For the case shown in Figure 3, the velocity magnitude diminishes by almost 80% when σ reaches $20R$, which is about twice as large as the tip height, and the same reduction percentage is achieved at the location $\sigma = 10R$ for the case with the narrow tip shown later in Figure 7. Note that both the velocity contours and the streamlines express the continuity of the velocity distribution and the viscous stress jump across the

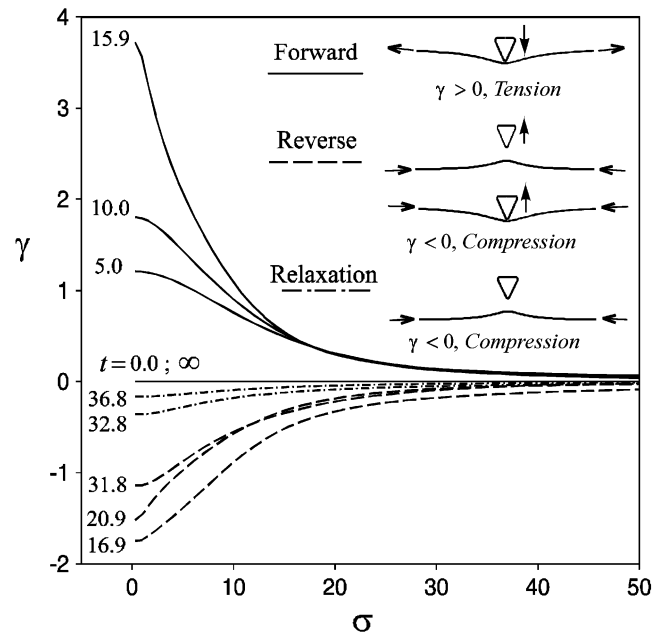


Figure 4. Isotropic local tension/compression force of the deforming membrane with bending rigidity $B = 1.0$ and spontaneous curvature $c_0 = -2.0$ probed by the AFM tip with an opening angle $\alpha = 60^\circ$.

infinitesimally thin membrane interface. The stress jump becomes more significant as the membrane elasticity and the membrane tension force increase around the membrane center where the membrane bending is the greatest.

Figure 4 depicts the local isotropic tension ($\gamma > 0$) or compression ($\gamma < 0$) forces acting on the membrane with respect to the radial position during forward, reverse, and relaxation modes of operation. When the AFM tip is moving forward, the membrane is pushed down by the fluid flow and the tension force is induced to drag the membrane into the center area to satisfy the surface area constraint imposed by the membrane incompressibility (eq 28). In the reverse motion, compression is observed as the membrane is pulled back and forced to adopt a new shape with the smaller area. Even when the membrane recedes over its neutral equilibrium position in the reverse motion (Figure 2), the surface force is still in the compression mode because the strong hydrodynamic forces overcome the force induced by the slow membrane self-relaxation, thereby maintaining the compression state of the membrane on a shorter time scale.

Figure 5 shows the instantaneous maximum deformation of the membrane (at the center) as a function of the instantaneous tip–membrane separation distance in a full cycle simulation. Clearly, this plot is analogous to the typical sampling force (proportional to membrane deformation) versus distance curves obtained experimentally during actual AFM imaging of biological cells. The range of experimentally measured bending rigidity values reported in the literature is 1.3×10^{-20} to 7×10^{-19} J with the nominal value about 10^{-19} J,^{29–32} which translates into parameter B values ranging between 0.1 and 20. The greater bending rigidity translates into stronger membrane resistance to deformation, as demonstrated by the smaller variation range for the trace curve along the y -axis.

- (29) Evans, E.; Rawicz, W. *Phys. Rev. Lett.* **1990**, *64*, 2094–2097.
- (30) Evans, E.; Rawicz, W. *Phys. Rev. Lett.* **1997**, *79*, 2379–2382.
- (31) Scheffer, L.; Bitler, A.; Ben-Jacob, E.; Korenstein, R. *Eur. Biophys. J.* **2001**, *30*, 83–90.
- (32) Döbereiner, H.-G.; Evans, E.; Kraus, M.; Seifert, U.; Wortis, M. *Phys. Rev. E* **1997**, *55*, 4458–4474.

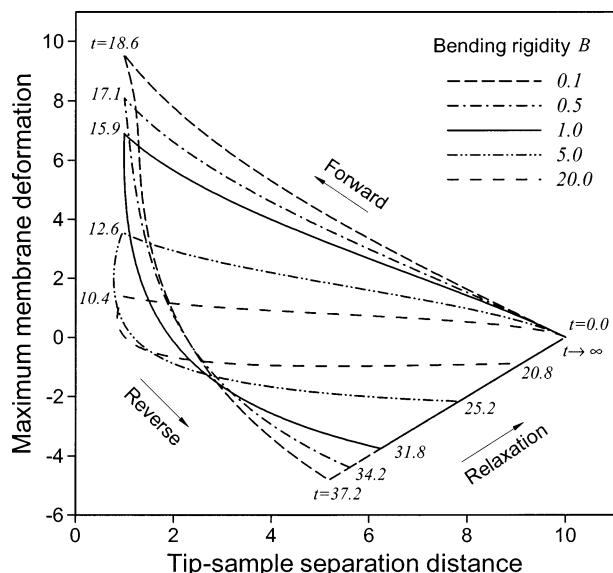


Figure 5. Effect of the bending rigidity on the hysteresis curve of the membrane deformation vs tip-sample separation distance for the membrane with spontaneous curvature $c_0 = -2.0$ and the AFM tip opening angle $\alpha = 60^\circ$.

At the same time, during the reverse operation mode and when the bending rigidity is sufficiently large, the membrane initially moves faster than an AFM tip, owing to the strong bending force acting on the membrane. This fact is manifested in Figure 5 by a decrease of the tip-membrane separation distance below 1.0 at the time moment just past 12.6, for the case of $B = 5.0$. The lagging response is also observed when the minimum tip-membrane separation distance (equal to 1.0) is maintained at times $t = 18.6, 17.1, 15.9, 12.6$, and 10.4 for the cases with bending rigidity $B = 0.1, 0.5, 1.0, 5.0$, and 20.0 , respectively. In the AFM imaging experiments, such an irreversible "hysteresis" behavior in respect to the forward and reverse motion of an AFM tip is frequently observed for soft samples, and our simulations provide the *first theoretical evidence* that this behavior is due to coupling of hydrodynamic and elastic membrane effects. Also, in the forward operation mode, as the tip approaches the membrane, the tip-sample interaction becomes stronger, and this results in a locally increased slope of the deformation curves when the tip-membrane separation distance approaches unity. The slope also appears much greater (i.e., a steeper change in the membrane deformation) in the beginning of the tip reverse motion due to contributions from both the bending force acting in the upward direction and the upward hydrodynamic pull force induced by the reverse motion of the AFM tip. After passing through the equilibrium membrane position with zero bending energy, the bending force begins to act in the opposite direction relative to the hydrodynamic force, leading to a decrease in the slope of deformation curves continuously until the AFM tip comes to rest at its upper elevated position. Finally, in the membrane relaxation mode, the deformation curves for all three bending rigidities are identical and the membrane relaxes to its equilibrium position, as expected, featuring a linear dependence on the tip-membrane separation distance.

In the AFM probing experiments, choosing the tip geometry is based on the characteristics of the sample surface and the requirements of the image resolution. Two of the most important factors affecting the image resolution

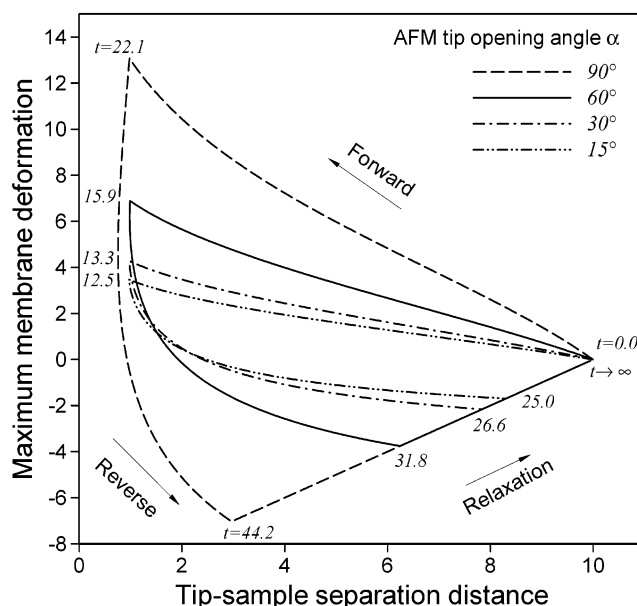


Figure 6. Effect of the AFM tip opening angle on the hysteresis curve of the membrane deformation vs tip-sample separation distance for the membrane with bending rigidity $B = 1.0$ and spontaneous curvature $c_0 = -2.0$.

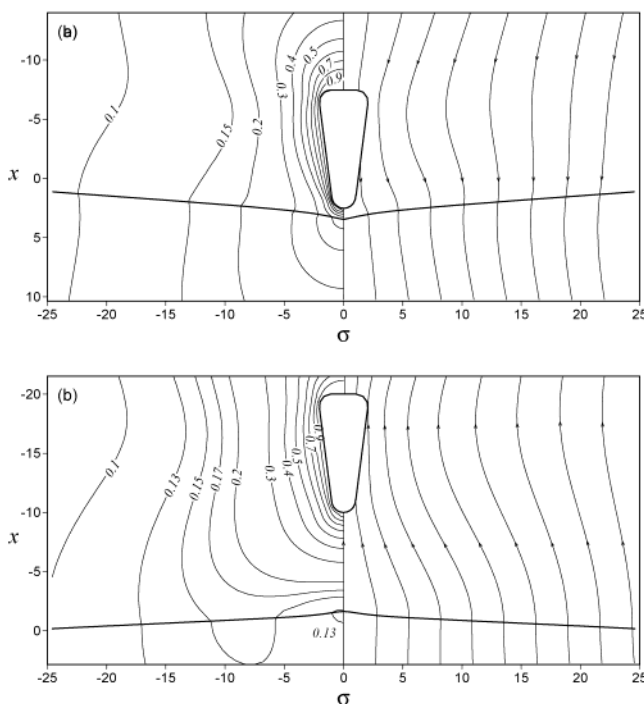


Figure 7. Instantaneous normalized velocity contours and streamlines around the AFM tip and the cell membrane at the following time instants: (a) $t = 12.5$ in the forward direction and (b) $t = 25.0$ in the reverse direction for the membrane with bending rigidity $B = 1.0$, spontaneous curvature $c_0 = -2.0$, and the AFM tip with an opening angle $\alpha = 15^\circ$.

are the tip sharpness (represented by the tip radius R) and the tip aspect ratio (represented by the tip opening angle α). Since our system is made dimensionless using the tip radius as a scale, the effect of the tip radius R is reflected in Figures 2–5. The effects of the tip opening angle are presented in Figures 6 and 7. Figure 6 illustrates the hysteresis plot for four different cases with the opening angle ranging from 15° to 90° . Clearly, a decrease in the AFM tip opening angle (tip sharpening) results in significant enhancement of the AFM sensitivity, as even

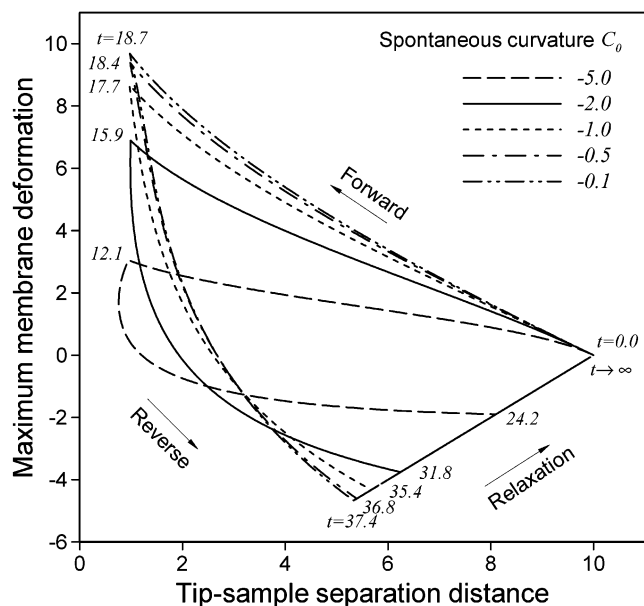


Figure 8. Effect of the spontaneous membrane curvature on the hysteresis curve of the membrane deformation vs tip-sample separation distance for the membrane with bending rigidity $B = 1.0$ and the AFM tip with an opening angle $\alpha = 60^\circ$.

small membrane deformation leads to a fairly large change in the separation distance between the tip and the cell membrane (Figure 6). This is because sharpening of the tip results in focusing of the hydrodynamic push/pull force into a much smaller region of the membrane, as illustrated by a decrease in size of the induced fluid flow domain and, in turn, much greater local velocity gradients in the flow field exemplified by the velocity contours and streamlines in Figure 7. In some sense, the effect of tip sharpening (Figure 6) is equivalent to an increase in the apparent bending rigidity of the membrane (Figure 5), which results in enhanced spatial resolution and sensitivity of the imaging process. Further, the duration of the full probing cycle decreases, thereby allowing for an increase in speed of the membrane scanning process.

Previous studies^{25,26} for the elastic properties of giant vesicles indicate that the bending rigidity of the membrane B serves only as a scaling factor for the membrane curvature effect (see eq 17), whereas the spontaneous curvature c_0 controls the equilibrium shape of the vesicles. Indeed, the spontaneous curvature represents a phenomenological constant to accommodate various effects due to the asymmetric fluid environment inside and outside of the cell and in the lipid bilayer structure of the membrane. It is obtained by fitting the experiment data of the equilibrium vesicle shape to the curvature elasticity model as shown in Deuling and Helfrich's work.³³ For example, they showed that a red blood cell features a shape of a biconcave disk with negative spontaneous curvatures. Although the elasticity model³³ does not impose any restrictions on the sign of the spontaneous curvature, the positive c_0 is rarely, if ever, found in the experiments. Our simulations show that positive spontaneous curvatures c_0 result in physically unrealistic results, for example, with the bending elastic force further augmenting the hydrodynamic push force in the forward operation mode. Thus, we only present the results for the negative spontaneous curvature by varying c_0 over a broad range from -0.1 to -5.0 , which corresponds to the values found in the experiments with giant vesicles and red blood cells.^{26,32,33} Figure 8 shows the hysteresis

curves that reflect the effect of the membrane spontaneous curvature. Clearly, with a decrease in the absolute value of c_0 , the maximum membrane deformation increases until it reaches the saturation limit at $c_0 \rightarrow 0$. The "hysteresis" curves shown in Figure 8 exhibit a qualitatively similar behavior to that of the "hysteresis" curves shown in Figure 5, which expresses the effect of another elastic constant, the bending rigidity B . Therefore, in practical applications, consolidating these two elastic constants, B and c_0 , may provide a basis for the simplified curvature elasticity model to be used as the dynamic boundary condition (eq 19) for interpretation of AFM images using analytical techniques.

5. Conclusions

The hydrodynamic interactions during AFM imaging of biological membranes have been investigated through fundamental theoretical analysis and numerical simulations. The model developed couples the Stokes flow induced by an AFM tip motion and the elastic membrane dynamics extended from Helfrich's theory.⁸ The governing conservation equations are solved by the boundary element method. In the calculations, the molecular level interactions are disregarded by keeping an AFM tip sufficiently far away from the membrane. The details of the membrane transient deformation and fluid motion (inside and outside of the cell) are described for three probing regimes: forward motion, reverse motion, and relaxation. In each case, a number of interesting and sometimes counterintuitive phenomena were observed such as (a) dominance of the compression force acting on the membrane in the reverse (pull-back) mode of AFM operation even after the membrane passes its equilibrium planar state; (b) a local instantaneous decrease in separation between the AFM tip and the membrane in the beginning of the reverse mode operation when the bending rigidity of the membrane is sufficiently large; (c) the tip parameters (the radius of curvature and the opening angle) define the sensitivity, resolution, and speed of the imaging process; and (d) the probing cycle lasts longer in the case of a softer membrane with smaller bending rigidity and smaller spontaneous curvature as well as when the AFM tip opening angle is large. The "hysteresis" behavior observed in the full cycle noncontact probing experiments using AFM for imaging soft biological samples has been explained by the strong coupling of hydrodynamic effects (fluid motion) and elastic deformation of the membrane when imaging takes place in the liquid environment. Our numerical results show that the highest tensile force (scaled by $V_0\mu$) induced by the fluid motion is of the order of 10^{-3} mN/m, which falls in the range of values measured in the micropipet experiments.³⁰ The predicted tensile force is also far below the observed rupture tension force of ~ 10 mN/m,³⁰ indicating that the induced viscous stress will not damage the cell membrane.

Our ongoing work focuses on incorporating the effect of the chemical species/ion transport driven by the diffusion process due to the gradient of the electrochemical potential across a permeable membrane. The ultimate goals are to augment the rudimentary Hertz model⁷ currently used to obtain the mechanical properties of the cells in the AFM-based experiments and also to develop a sound theoretical framework for interpretation of experimental information obtained using multifunctional (i.e., combined AFM, SECM, and SNOM) scanning probes for imaging a broad range of biological samples.

Acknowledgment. The authors are grateful for the financial support of this work from the National Science Foundation and Georgia Institute of Technology. Special

(33) Deuling, H. J.; Helfrich, W. *Biophys. J.* **1976**, *16*, 861–868.

thanks also go to Drs. B. Mizaikoff, C. Kranz, and A. Kueng (Department of Chemistry, Georgia Tech) for fruitful discussions on the AFM probing experiment.

Appendix

In terms of the Green's function expressed in the Cartesian coordinates, the transformation matrices are given by¹⁰

$$M_{\alpha\beta} = \sigma \int_0^{2\pi} \begin{bmatrix} G_{xx} & G_{yx} \cos \phi + G_{zx} \sin \phi \\ G_{xy} & G_{yy} \cos \phi + G_{zy} \sin \phi \end{bmatrix} d\phi$$

$$Q_{\alpha\beta} = \sigma \int_0^{2\pi} \begin{bmatrix} T_{xxx} & T_{yxx} \cos \phi + T_{zxx} \sin \phi \\ T_{xyx} \cos \phi + T_{xxz} \sin \phi & T_{yyx} \cos^2 \phi + T_{zzx} \sin^2 \phi + 2T_{yzz} \cos \phi \sin \phi \end{bmatrix} d\phi$$

$$Q_{\alpha\beta} = \sigma \int_0^{2\pi} \begin{bmatrix} T_{yxx} & T_{yyx} \cos \phi + T_{zyx} \sin \phi \\ T_{xyy} \cos \phi + T_{xyz} \sin \phi & T_{yyy} \cos^2 \phi + T_{yyz} \sin^2 \phi + 2T_{yyz} \cos \phi \sin \phi \end{bmatrix} d\phi$$

After simplifications, the elements of the transformation matrices are given by

$$\begin{aligned} M_{xx} &= \sigma(I_{10} + \hat{x}^2 I_{30}), \quad M_{xx} = \hat{x}\sigma(\sigma I_{30} - \sigma_0 I_{31}), \\ M_{ox} &= \hat{x}\sigma(\sigma I_{31} - \sigma_0 I_{30}), \\ M_{\sigma\sigma} &= \sigma[I_{11} + (\sigma^2 + \sigma_0^2)I_{31} - \sigma\sigma_0(I_{30} + I_{32})], \\ Q_{xxx} &= -6\hat{x}^3\sigma I_{50}, \quad Q_{xx\sigma} = -6\hat{x}^2\sigma(\sigma I_{50} - \sigma_0 I_{51}), \\ Q_{x\sigma x} &= Q_{x\sigma\sigma}, \quad Q_{x\sigma\sigma} = -6\hat{x}\sigma(\sigma^2 I_{50} + \sigma_0^2 I_{52} - 2\sigma\sigma_0 I_{51}), \\ Q_{\sigma xx} &= -6\hat{x}^2\sigma(\sigma I_{51} - \sigma_0 I_{50}), \quad Q_{\sigma\sigma x} = Q_{\sigma\sigma\sigma}, \\ Q_{x\sigma x} &= -6\hat{x}\sigma[(\sigma^2 + \sigma_0^2)I_{51} - \sigma\sigma_0(I_{50} + I_{52})], \\ Q_{\sigma\sigma\sigma} &= -6\sigma[\sigma^3 I_{51} - \sigma^2\sigma_0(I_{50} + 2I_{52}) + \\ &\quad \sigma\sigma_0^2(I_{53} + 2I_{51}) - \sigma_0^3 I_{52}] \end{aligned}$$

where $\mathbf{x}_0 = (x_0, \sigma_0)$, $\hat{x} = x - x_0$, and the integrals I_{ij} are derived from the Integral Tables³⁴ in terms of complete elliptic integrals:

$$\begin{aligned} I_{10} &= \frac{2k}{(\sigma\sigma_0)^{1/2}} F, \quad I_{11} = \frac{2}{(\sigma\sigma_0)^{1/2}} k [(2 - k^2)F - 2E], \\ I_{30} &= \frac{k^3 E}{2(\sigma\sigma_0)^{3/2} (1 - k^2)}, \\ I_{31} &= \frac{k}{(\sigma\sigma_0)^{3/2}} \left[\frac{2 - k^2}{2(1 - k^2)} E - F \right], \\ I_{32} &= \frac{1}{(\sigma\sigma_0)^{3/2}} k \left[\frac{k^4 - 8k^2 + 8}{2(1 - k^2)} E + (2k^2 - 4)F \right], \\ I_{50} &= \frac{k^5}{24(\sigma\sigma_0)^{5/2} (1 - k^2)} \left[\frac{2(2 - k^2)}{1 - k^2} E - F \right], \\ I_{51} &= \frac{k^3}{24(\sigma\sigma_0)^{5/2} (1 - k^2)} \left[\frac{2(k^4 - k^2 + 1)}{1 - k^2} E + \right. \\ &\quad \left. (k^2 - 2)F \right], \\ I_{52} &= \frac{k}{24(\sigma\sigma_0)^{5/2} (1 - k^2)} \left[\frac{2(-k^6 + 6k^2 - 4)}{1 - k^2} E - \right. \\ &\quad \left. (k^4 + 8k^2 - 8)F \right], \\ I_{53} &= \frac{l}{24(\sigma\sigma_0)^{5/2} (1 - k^2)} k \\ &\quad \left[\frac{2(k^8 + k^6 - 33k^4 + 64k^2 - 32)}{1 - k^2} E + \right. \\ &\quad \left. (k^6 + 30k^4 - 96k^2 + 64)F \right] \end{aligned}$$

The complete elliptic integrals of the first and second kind and the modulus are defined by, respectively,

$$\begin{aligned} F(k) &= \int_0^{\pi/2} \frac{d\theta}{\sqrt{1 - k^2 \sin^2 \theta}}, \\ E(k) &= \int_0^{\pi/2} \sqrt{1 - k^2 \sin^2 \theta} d\theta, \quad k^2 = \frac{4\sigma\sigma_0}{\hat{x}^2 + (\sigma + \sigma_0)^2} \end{aligned}$$

(34) Gradshteyn, I. S.; Ryzhik, I. M. *Table of Integrals, Series, and Products*; Academic Press: 1980.